HOKKAIDO UNIVERSITY

Title	Superconductivity in noncentrosymmetric Ag2Pd3S
Author(s)	Yoshida, H.; Okabe, H.; Matsushita, Y. et al.
Citation	Physical Review B, 95(18), 184514 https://doi.org/10.1103/PhysRevB.95.184514
Issue Date	2017-05-22
Doc URL	https://hdl.handle.net/2115/66433
Rights	©2017 American Physical Society
Type	journal article
File Information	PhysRevB95 184514.pdf

Hokkaido University Collection of Scholarly and Academic Papers : HUSCAP

Superconductivity in noncentrosymmetric Ag_2Pd_3S

H. Yoshida,[1,2,*] H. Okabe,[1] Y. Matsushita,[1] M. Isobe,[1] and E. Takayama-Muromachi[1]
[1]*National Institute for Materials Science, 1-1 Namiki, Tsukuba, Ibaraki 305-0044, Japan*
[2]*Department of Physics, Faculty of Science, Hokkaido University, Sapporo, Hokkaido 060-0810, Japan*
(Received 10 January 2015; revised manuscript received 3 May 2017; published 22 May 2017)

We have successfully synthesized the single crystal of Ag_2Pd_3S, which exhibits superconductivity with the transition temperature of $T_c = 2.25$ K. Ag_2Pd_3S crystallizes in the space group $P4_132$ with the filled β-Mn structure, which has no inversion symmetry. The value of the Ginzburg-Landau parameter κ_{GL} indicates that Ag_2Pd_3S is a type-II superconductor. $\Delta C(T_c)/\gamma_n T_c = 1.50$ and $2\Delta/k_B T_c = 3.48$ from the heat-capacity analyses indicate that Ag_2Pd_3S is a weak-coupling Bardeen-Cooper-Schrieffer (BCS) superconductor with an isotropic superconducting gap. On the other hand, the violation of the Werthamer-Helfand-Hohenberg curve in the H-T phase diagram implies Ag_2Pd_3S is not a typical BCS superconductor.

DOI: 10.1103/PhysRevB.95.184514

Noncentrosymmetric superconductors (NCSCs), whose crystal structures lack inversion symmetry, have recently attracted much attention due to their potential to realize unconventional superconductivity [1]. The Cooper-pair wave function of conventional superconductors generally consists of the product of orbital (i.e., $s-$, $p-$, or d-wave) and spin (singlet or triplet) parts. The combinations of these parts are strictly determined by the parity symmetry; if the orbital part is s wave, the spin part is definitely singlet (even parity). However, this rule does not apply to NCSCs. The large antisymmetric spin-orbit coupling (ASOC) of NCSCs induces the mixing of orbital and spin parts, resulting in a mixture of the spin-singlet and spin-triplet states [2,3].

Triggered by the discovery of exotic superconductivity in $CePt_3Si$ [4], extensive experimental and theoretical investigations on NCSCs have been carried out to understand their advantageous properties. $CePt_3Si$ has an unusually high upper critical field $H_{c2} = 4 \sim 5$ T, which significantly exceeds the Pauli limit for singlet superconductivity ($H_{c2} \sim 1$ T). In addition, NSCSs are predicted to exhibit some other exotic phenomena, such as anisotropic superconducting gap structures and unique magnetoelectric effects that derive from their polar symmetry [5–10].

Recently, a number of compounds have been investigated as candidates for NCSCs [11–24], such as $CePt_3Si$ [4] and $CeRhSi_3$ [11]. These two compounds have been extensively studied by many researchers, leading to the discovery of an unusual symmetry present in the Cooper pairs. $CePt_3Si$ and $CeRhSi_3$ belong to the category of heavy fermion superconductors. In these superconductors, not only the broken inversion symmetry but also the quantum criticality affect the superconductivity of the compounds.

On the other hand, Li_2M_3B (M = Pd,Pt) [14–24] are two of the appropriate compounds for forming NCSCs to investigate effects of the broken spatial inversion symmetry only. Li_2M_3B (M = Pd,Pt) do not contain any magnetic elements; therefore, effects of magnetic ordering can be completely ignored. In this system, superconducting properties are directly dependent on the magnitude of ASOC. Li_2Pt_3B exhibits unconventional superconductivity with an anisotropic superconducting gap structure; ^{11}B NMR experiments and magnetic penetration depth measurements revealed that the Cooper pair included about 60% of the spin-triplet pairing and 40% of the spin-singlet pairing, and the energy gap had a line node. In contrast, the gap structure of Li_2Pd_3B has been under debate. An isotropic full gap structure is suggested by various bulk measurements such as heat capacity [16,17], whereas Yuan *et al.* claimed by magnetic penetration depth measurements that a multigap structure consist of two gaps in which one is dominant and the other is small enough not to affect the obtained gap structure by bulk heat-capacity measurements [18]. On the other hand, Yuan *et al.* also pointed out by precise fitting of the temperature dependence of magnetic penetration depth below T_c that the gap is slightly anisotropic and there existed two gaps which had almost the same size [20]. The magnitude of ASOC of Pt is somewhat larger than that of Pd, and this should cause the two compounds to demonstrate different types of superconductivity.

In this study, we focused on the ternary compound Ag_2Pd_3S. The superconductivity of Ag_2Pd_3S ($T_c = 1.13$ K) was first reported by Khan *et al.* in 1973 [25]. They synthesized a polycrystalline sample of Ag_2Pd_3S and found superconductivity by measuring an electrical resistivity. Thirty years later, Schaak *et al.* reported that Ag_2Pd_3S could be synthesized by the rapid low-temperature solution method [26]. However, details of the crystal structure have not been completely resolved due to the difficulty of structural analysis of polycrystalline samples, although the basic crystal structure of Ag_2Pd_3S was expected to be the β-Mn-type structure [25,26]. In addition, superconducting properties also remain poorly understood.

We have successfully synthesized single crystals of Ag_2Pd_3S. Detailed structural analyses were performed using the single-crystal samples, and it was revealed that Ag_2Pd_3S crystallized in a filled β-Mn-type structure with space group $P4_132$. This is isostructural to Li_2M_3B (M = Pd,Pt; space group $P4_332$), but these two structures have different types of crystallographic chirality: Ag_2Pd_3S has a right-handed structure, and Li_2M_3B has a left-handed structure. The superconductivity in Ag_2Pd_3S is of interest due to the similarity of its crystal structure with that of Li_2Pt_3B, since Li_2Pt_3B exhibits unconventional superconductivity in terms of the absence of the inversion symmetry. The studies of Ag_2Pd_3S,

*hyoshida@sci.hokudai.ac.jp

 ©2017 American Physical Society

TABLE I. Details of single-crystal x-ray diffraction data collection and crystal refinement results for Ag_2Pd_3S.

Compound	Ag_2Pd_3S
Formula weight	567.1 g mol^{-1}
Color, shape	Metallic luster, cuboid
Crystal dimension	0.1 × 0.08 × 0.06 mm^3
Temperature	293 K
Space group	$P4_132$
a	7.2292(2) Å
Volume	377.81(3) Å^3
Z	4
D_e	9.968 g m^{-3}
F(000)	992
Absorption coefficient	24.491 mm^{-1}
Radiation	Mo $K\alpha$ (0.71073 Å)
Range of h,k,l	$h: -12/12$, $k: -11/13$, $l: -12/13$
Refelections collected	8862
Independent reflections	417
Refelctions with $I > 2\sigma(I)$	408
$R_{obs}(F)$	0.0181
$wR_{all}(F^2)$	0.0324
Goodness of fit	1.31

an appropriate candidate compound for a NCSC, can be of significant importance for understanding physical properties of superconductors without inversion symmetry. In this paper, we investigate details of the crystal structure and superconducting properties of Ag_2Pd_3S and discuss similarities to other NSCSs, especially $Li_2M_3B(M = Pd,Pt)$.

The single-crystal samples were prepared by a self-flux method. The starting materials of Ag_2S and a fine powder of Pd metal were mixed in the molar ratio 1:3 and then pressed into a pellet. The pellet was sealed in an evacuated quartz tube and heated at 1000 °C for 48 h. After slowly cooling down to 500 °C at a rate of 5 °C/h, it was then quenched to room temperature. The obtained samples were in the form of a chunk of single crystals with a metallic luster. No interdomain impurity was confirmed by powder x-ray diffraction using pulverized crystals.

A single-crystal x-ray diffraction experiment at 293 K was carried out with a Bruker SMART APEX single-crystal diffractometer with a charge-coupled device area detector using Mo $K\alpha$ radiation. The intensity data were integrated using SAINT and SADABS was employed to correct for absorption effects [27]. The structural parameters were refined using the program SHELXL-2013 based on the full-matrix method [28]. The final reliability indexes (R values) were $R_{obs}(F) = 1.81\%$ and ${}_wR_{all}(F^2) = 3.24\%$. The details of the single-crystal x-ray diffraction measurement are summarized in Table I. The chemical composition of the crystal was confirmed to be almost stoichiometric using electron probe microanalysis.

The electrical resistivity was measured with a conventional dc four-probe method on a shaped lump of the single crystals in the temperature range 0.5–300 K using a Quantum Design (QD) Physical Properties Measurement System (PPMS). Heat-capacity measurements were carried out between 0.4 and 300 K using the heat-relaxation method on the lump of the single crystals in the QD PPMS. Magnetic susceptibility data were collected using a powder sample obtained from the pulverized crystal in the temperature range 1.8–300 K using a superconducting quantum interference device magnetometer (QD Magnetic Properties Measurement System).

TABLE II. Structural parameters of Ag_2Pd_3S and Li_2Pd_3B [15].

Atom	Site	X	Y	z	Occupation
			Ag_2Pd_3S		
Ag	8c	0.05744(4)	0.05744(4)	0.05744(4)	1
Pd	12d	0.125	0.19446(4)	0.44446(4)	1
S	4a	0.375	0.375	0.375	1
			Li_2Pd_3B		
Li	8c	0.3051(3)	0.3051(3)	0.3051(3)	1
Pd	12d	0.125	0.3043(1)	−0.0543(1)	1
B	4a	0.625	0.625	0.625	1

First-principles calculations with spin-orbit coupling were carried out using the full-potential linearized augmented plane-wave (FLAPW) method, as implemented in the WIEN2K program package [29]. The Perdew-Burke-Ernzerhof generalized gradient approximation (GGA) potential was used for the exchange-correlation potential [30]. Experimentally obtained values for lattice constants and internal coordinates (see Table II) were used in our calculations. The linearized augmented plane-wave sphere radii of Ag_2Pd_3S were set to 2.50 a.u. for Ag, 2.28 a.u. for Pd, and 2.02 a.u. for S. The cutoff parameter $R_{MT}K_{max}$ was chosen as 8.0, where R_{MT} is the radius of the Ag sphere and K_{max} is the magnitude of the largest reciprocal lattice vector. Self-consistency was imposed on k-point meshes of 94 points (12 × 12 × 12; we used approximately 1800 special k points) in the irreducible part of the Brillouin zone.

The crystal structure of Ag_2Pd_3S is illustrated in Fig. 1(a). The details of structural parameters and the anisotropic atomic displacement parameters are shown in Tables II and III. Ag_2Pd_3S crystallizes in space group $P4_132$, and the lattice constant is a = 7.229 Å. The crystal structure is well described by the filled β-Mn structure. There are many intermetallic compounds that have a β-Mn structure, which originally possesses the A_2B_3 composition for the Mn metal, as shown in Fig. 1(b). In the A_2B_3-type structure, the 8c and 12d sites can be occupied by atoms, whereas the interstitial 4a site

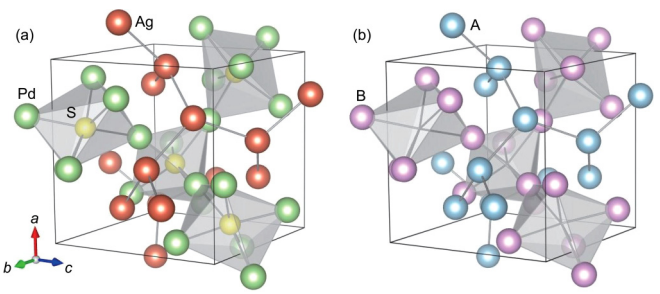

FIG. 1. (a) Crystal structure of Ag_2Pd_3S. Each shaded polyhedron represents a Pd_6S octahedron, in which sulfur is located at the center. The interstitial space in the Ag network is filled by corner-sharing Pd_6S octahedra. (b) Crystal structure of the A_2B_3 β-Mn structure. The solid line represents a cubic unit cell.

TABLE III. Anisotropic atomic displacement parameters U (Å) of Ag_2Pd_3S.

Atom	U_{iso}	U_{11}	U_{22}	U_{33}	U_{12}	U_{13}	U_{23}
Ag	0.01438(9)	0.01438(9)	0.01438(9)	0.01438(9)	0.00043(8)	0.00043(8)	0.00043(8)
Pd	0.01288(8)	0.01071(14)	0.01397(10)	0.00329(10)	0.00178(11)	0.00178(7)	−0.00178(7)
S	0.0101(3)	0.0101(3)	0.0101(3)	0.0101(3)	−0.0004(3)	−0.0004(3)	−0.0004(3)

is basically vacant. Notably, the β-Mn structure exhibits a flexible composition due to an accommodating atom C at the 4a site, such as in $(A,B)_5C$, $(A,B)_4C$, or $(A,B)_3C$, including defects at the 8c and 12d sites to satisfy the Hume-Rothery rules.

The filled β-Mn structure is the crystal structure in which all 4a, 8c, and 12d sites are fully occupied. In many cases, small atoms, such as carbon, boron, and nitrogen, can only be located at the interstitial 4a site. To the best of our knowledge, Ag_2Pd_3S is the first compound that includes a large sulfur atom at the 4a site. A feature of the structure is a three-dimensional network consisting of Ag atoms with corner-sharing Pd_6S octahedra that penetrate into the interspaces of the Ag network, as shown in Fig. 1. In the Ag network, all Ag atoms have three neighboring Ag atoms with the interatomic distance 2.74 Å, which is 0.15 Å shorter than that of Ag metal (2.89 Å). This suggests that an electron transfer occurs from Ag to the Pd/S framework.

The crystal structure of Ag_2Pd_3S is very similar to that of Li_2Pd_3B. However, the space group of Ag_2Pd_3S is $P4_132$, which is different from that of Li_2Pd_3B ($P4_332$). The corresponding crystallographic sites are as follows: S and B at 4a, Ag and Li at 8c, and Pd at the 12d site. The difference between these crystal structures lies in the helicity around the spiral axis. In Ag_2Pd_3S, atoms have right-handed helicity, while in Li_2Pd_3B, atoms are arranged with a left-handed helicity; in other words, the β-Mn structure has a degree of freedom of the structural chirality. It is known that the structural chirality sometimes affects the magnetic properties of localized spin systems [31,32]. On the other hand, it is unclear whether the chirality degree of freedom influences physical properties of metals, itinerant spin systems or not.

As shown in Fig. 2(a), the temperature dependence of the resistivity shows typical metallic behavior. The resistivity decreases with decreasing temperature, and the curve shows an upward convex feature at low temperatures. Zero resistivity was clearly observed below 2 K at zero magnetic field, indicating an occurrence of a superconducting transition. The transition temperature was determined from a zero and an onset of resistivity. The onset of resistivity is defined as a point where the linear extrapolation of the slope in the transition region intersects the linear extrapolation of the plateau region, as shown in the inset of Fig. 2(a). By applying magnetic fields, the transition is gradually broadened. Zero resistivity was not observed at or below 0.5 K under a magnetic field of $\mu_0 H = 1$ T, as shown in Fig. 2(b), resulting in the residual resistivity $\rho_0 = 6.21 \times 10^{-5}\,\Omega\,\mathrm{cm}$ and the residual resistivity ratio, $RRR \sim 5$ at $T = 0.55$ K.

Figure 3(a) shows the temperature dependence of the magnetic susceptibility under a magnetic field of 10 Oe. Single crystals were well ground to obtain powder samples, and measurements were performed on the polycrystalline samples. As shown in Fig. 3(a), the magnetic susceptibility shows diamagnetism below 2.2 K. This is evidence for superconductivity. The Meissner volume fraction estimated at 1.8 K under the field-cooled process is about 40%, indicating that the superconductivity is a bulk phenomenon.

The superconducting M-H curve measured at 1.8 K is shown in Fig. 3(b). The magnetic shielding effect clearly occurs below about 900 Oe at 1.8 K. The M-H curve strongly indicates that Ag_2Pd_3S is a type-II superconductor, which is a typical superconducting behavior with weak vortex pinning. The inset shows a magnified version of the low-magnetic-field region. The lower critical field H_{c1}, at which the magnetization

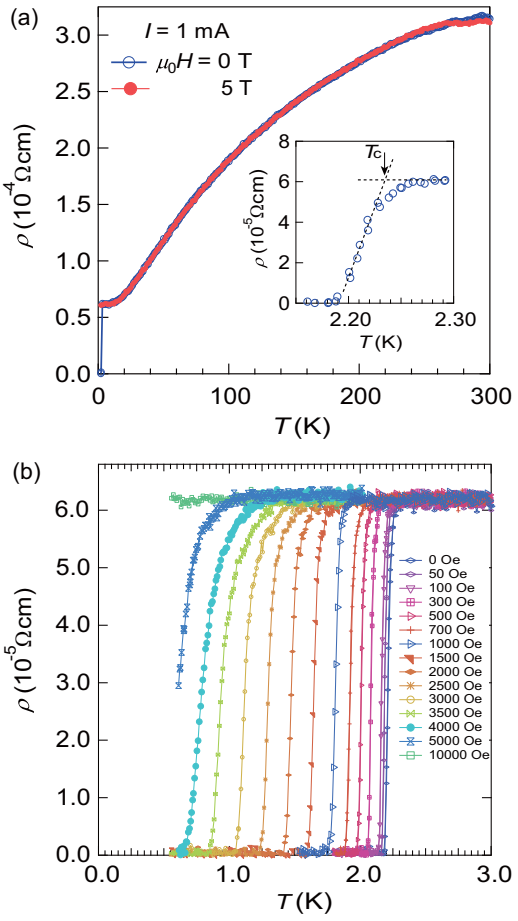

FIG. 2. (a) Temperature dependence of the resistivity of Ag_2Pd_3S up to 300 K under magnetic fields $\mu_0 H = 0$ and 1 T, and (b) resistivity between 0.5 and 3 K under various magnetic fields. The inset of (a) illustrates the definition of the transition temperature T_c and shows a magnified version of the region around the transition temperature. The arrow indicates the T_c estimated from the onset resistivity.

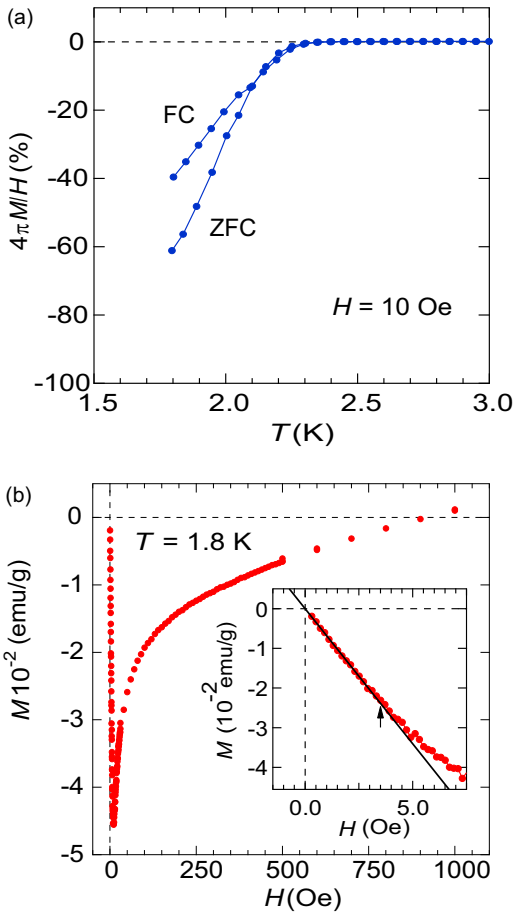

FIG. 3. (a) Temperature dependence of the magnetic susceptibility in Ag_2Pd_3S. The data for zero-field-cooled (ZFC) and field-cooled (FC) processes were plotted. (b) Magnetization vs magnetic field (M-H) curve for Ag_2Pd_3S. The inset of (b) shows the M-H curve in the low-magnetic-field region. The arrow indicates the lower critical field H_{c1} defined as the deviation field, which represents the deviation from the linear behavior of magnetization.

deviates from a linear response, was 3.5 Oe at 1.8 K, indicating that vortices can penetrate the compound at very low magnetic fields.

The temperature dependence of total heat capacity (electronic part and lattice part) C_{total}/T vs T^2 under $\mu_0 H = 0$ and 1 T is depicted in Fig. 4(a). A peak observed at zero magnetic field was completely suppressed at $\mu_0 H = 1$ T. The Sommerfeld coefficient γ and the phononic specific heat coefficient β were estimated as $\gamma = 8.55\,\text{mJ/(mol K}^2)$ and $\beta = 0.96\,\text{mJ/(mol K}^4)$. These values were obtained by a linear extrapolation to the normal heat capacity C_{total} under $\mu_0 H = 1$ T, assuming $C_{\text{total}} = \gamma T + \beta T^3$ equation. The Debye temperature $\Theta_D = 230$ K was also determined from the relation $\beta = (12/5)\pi^4 N_{\text{fu}} N_A k_B/{\Theta_D}^3$. Here, N_A is the Avogadro constant, N_{fu} is the number of atoms per formula unit, and k_B is the Boltzmann constant. We obtain the electron-phonon coupling constant $\lambda_{\text{el-ph}} = 0.48$ from McMillan's formula $T_c = (\Theta_D/1.45)\exp[-1.04(1+\lambda_{\text{el-ph}})/\{\lambda_{\text{el-ph}} - \mu^*(1+0.62\lambda_{\text{el-ph}})\}]$ [33] by substituting $\Theta_D = 230$ K and the Coulomb pseudopotential $\mu^* = 0.13$ [34]. The small value of $\lambda_{\text{el-ph}}$ suggests that a weak-coupling superconductivity is realized in this compound.

The temperature dependence of the electronic specific heat divided by temperature, $C_{\text{el}}/T = C_{\text{total}}/T - \beta T^2$, is illustrated in Fig. 4(b). We estimated the transition temperature $T_c = 2.25$ K and the jump of heat capacity $\Delta C(T_c)/T_c = 10.52$ at T_c to satisfy the entropy conservation around T_c. Figure 4(c) shows the temperature dependence of C_{el} at zero magnetic field. The thermodynamic critical field $\mu_0 H_c(0)$ estimated from the equation $\mu_0 H_c(0)/2 = -\gamma {T_c}^2/2 + \int_0^{T_c} C_{\text{el}}(T)\text{d}T$ is 0.018 T. We analyzed C_{el} below T_c to reveal the nature of a superconducting gap. The solid line shows the fitting result assuming the specific heat expression for a conventional superconductor with temperature-linear term $C_{\text{el}} = \gamma_0 T + a^* \exp\{-\Delta(0)/k_B T\}$, where $\Delta(0)$ is the energy gap. The estimated gap value is $\Delta(0)/k_B = 3.91$ K, and thus $2\Delta/k_B T_c$ is calculated to be 3.48. This is close to the value of 3.53 that is expected from the BCS theory. We obtained a finite value of $\gamma_0 = 1.53$ mJ/(mol K^2) at $T = 0$ K, suggesting that part of the domains in the Ag_2Pd_3S crystal does not participate in the superconductivity. It is probably due to internal defects in the Ag_2Pd_3S crystal, such as local inhomogeneity deviated slightly from the stoichiometric composition. Accordingly, the Sommerfeld coefficient of normal state intrinsic to the superconducting fraction should be $\gamma_n = \gamma - \gamma_0 = 7.02\,\text{mJ/(mol K}^2)$. Thus, the experimental value $\Delta C(T_c)/\gamma_n T_c = 1.50$ is consistent with that of the BCS weak-coupling limit value 1.43.

Figure 4(d) shows the temperature dependence of C_{el}/T under several magnetic fields. Transition temperatures under each field were determined by assuming entropy balance around T_c. Applying magnetic fields causes each peak to shift to a lower temperature. Finally, the peaks vanish above $\mu_0 H = 0.5$ T, indicating that the superconducting transition is suppressed under those magnetic fields. Note that the onset of the superconductivity was still observed in the temperature dependence of the resistivity at $\mu_0 H = 0.5$ T.

Figure 5 shows the total and partial density of states (DOS) of Ag_2Pd_3S including the spin-orbit coupling calculated by the FLAPW method. As shown in Fig. 5, we found that Ag_2Pd_3S possesses a finite DOS at the Fermi level, which is mainly composed of the Pd 3*d* orbital, while the contributions from Ag and S are small. The DOS structure we obtained is similar to that of Li_2Pd_3B calculated by Lee *et al.* [35]. The calculated DOS at E_F per formula unit (f.u.) is 9.51 states/eV f.u., and the Sommerfeld coefficient γ_{cal} evaluated from the DOS is 5.61 mJ/(mol K^2). This value is slightly smaller than that obtained experimentally: $\gamma_n = 7.02$ mJ/(mol K^2). The mass enhancement may be attributed to the electron-phonon and electron-electron interactions.

Figure 6 summarizes the temperature dependence of the upper critical field H_{c2} in Ag_2Pd_3S deduced from resistivity and heat-capacity measurements. T_c values under several magnetic fields are estimated from both onset and zero resistivity, and from the C_{el}/T vs T plot. T_c estimated from the heat capacity nearly corresponds to that from the onset of resistivity. Thus, we estimate the upper critical field using the plots of the onset of resistivity. The Werthamer-Helfand-Hohenberg (WHH) model for the H_{c2} in the dirty

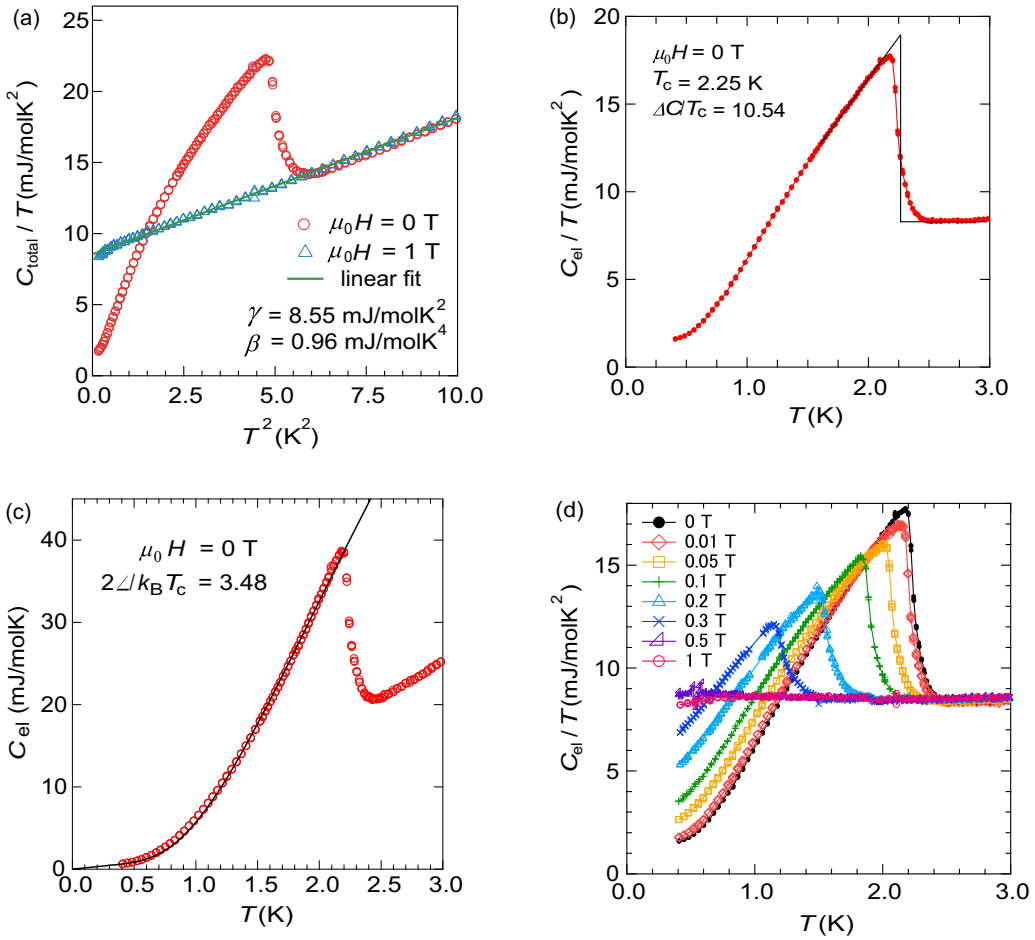

FIG. 4. (a) Temperature dependence of the total heat capacity under magnetic fields $\mu_0 H = 0$ and 1 T in the $C_{\rm total}/T$ vs T^2 plot. The solid line indicates the result of fitting to the conventional equation $C/T = \gamma + \beta T^2$. (b) Temperature dependence of the electron part of the heat capacity, $C_{\rm el}$, divided by the temperature at zero field. The T_c value is determined by requiring conservation of the entropy balance around the heat capacity jump. (c) Electronic heat capacity in the $C_{\rm el}$ vs. T plot at zero field. The solid line shows the result of fitting to $C_{\rm el} = \gamma_0 T + a^* \exp\{-\Delta(0)/k_B T\}$. (d) Electronic heat capacity divided by temperature under several magnetic fields: $\mu_0 H = 0, 0.01, 0.05, 0.1, 0.2, 0.3$, and 1 T.

limit, $\mu_0 {H_{c2}}^{\rm WHH}(0) = -0.693\, T_c |d(\mu_0 H_{c2})/dT|_{Tc} = 0.43$ T [36–38], is used to fit the H-T curve. However, we were unable to reproduce the experimental results, especially in low-temperature and high-magnetic-field regions. Thus, we determined an approximated value of the upper critical field $\mu_0 H_{c2}(0) \sim 0.63$ T from a linear extrapolation at around T_c. According to the BCS theory, the $H_{c2}(0)$ value is related to the coherence length ξ by $H_{c2}(0) = \phi_0/2\pi\xi(0)^2$, where ϕ_0 is the magnetic flux quantum. Using this formula, we obtain the value $\xi(0) = 23$ nm. The Ginzburg-Landau parameter $\kappa_{\rm GL}$ and the penetration depth $\lambda(0)$ are estimated from the relations $\mu_0 H_{c2}(0) = \sqrt{2}\kappa_{\rm GL}\mu_0 H_c(0)$ and $\kappa_{\rm GL} = \lambda(0)/\xi(0)$. We obtain the values $\kappa_{\rm GL} = 25$ and $\lambda(0) = 568$ nm, respectively. These parameters from the experiments are summarized in Table IV.

The value $T_c = 2.25$ K for Ag_2Pd_3S is about two times larger than values previously reported [25,26]. Since we were unable to prepare samples that have a lower transition temperature in this research, it is hard to understand experimentally why the T_c values are different from each other. One possible explanation is an influence of the sulfur deficiency of the previous studies, which may be caused by the large surface area due to the polycrystalline samples. The DOS structure of Ag_2Pd_3S shown in Fig. 5 may shed light on the difference in the T_c values of those two samples. The DOS of Ag_2Pd_3S obtained from the band calculation exhibits steep peaks around E_F. If the system obeys a rigid band scheme, a small amount of sulfur deficiency decreases the carrier electron content and leads to the reduction of the DOS at E_F (E_F shifts to a lower energy). In the BCS theory, T_c directly relates to the DOS at E_F; therefore, this reduction of DOS may significantly affect the magnitude of T_c. On the other hand, we used single-crystalline samples in our experiment. The chemical analysis and the single-crystalline x-ray diffraction measurement ensure that there is negligible sulfur deficiency in our samples. This may cause the larger DOS at E_F compared to those of previous samples, resulting in our higher T_c.

The results of bulk measurements of Ag_2Pd_3S suggest that superconducting properties of the compound are described by the conventional BCS model; thermodynamic analyses of $\Delta C(T_c)/\gamma_n T_c = 1.50$ and $2\Delta/k_B T_c = 3.48$ correspond to the usual single full-gap picture. Comparing with related compounds Li_2M_3B(M = Pd, Pt), the superconductivity of Ag_2Pd_3S is close to that of Li_2Pd_3B. Previous reports reveal

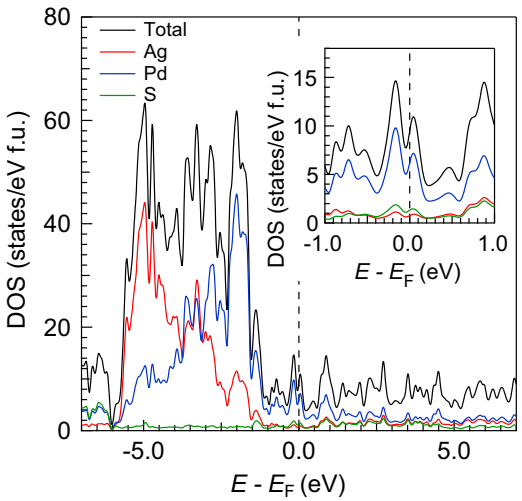

FIG. 5. Calculated DOS of Ag_2Pd_3S with spin-orbit interaction. The total and partial DOS for each atom is illustrated. The broken line at $E = 0$ indicates the Fermi energy.

that admixture of the spin-singlet and the spin-triplet states with a line node in a superconducting gap is realized in Li_2Pt_3B, while the detailed gap structure of Li_2Pd_3B is unsolved; the possibilities of an isotropic single gap and a two-gap structure has been under discussion [18,20]. The differences in the superconducting properties between Li_2Pd_3B and Li_2Pt_3B are attributed to the magnitude of ASOC of each compound. A larger value of ASOC should be responsible for the unconventional superconductivity of Li_2Pt_3B, since they have similar crystal structures and electron-phonon coupling constants $\lambda_{\text{el-ph}}$ [23,24,34]. In Ag_2Pd_3S, the relatively weak ASOC affects the electronic structure and

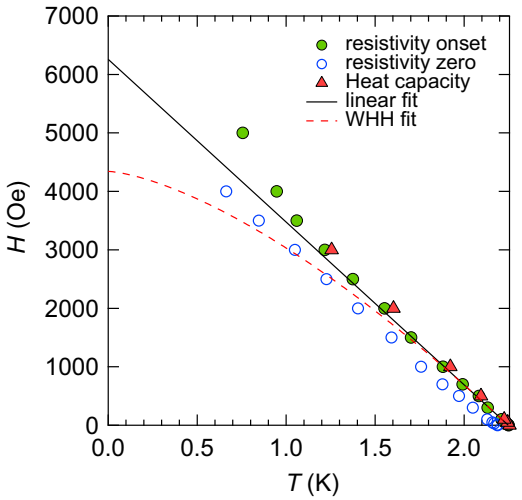

FIG. 6. H-T phase diagram of Ag_2Pd_3S deduced from the temperature dependence of the resistivity and heat capacity. The solid and open circles indicate the T_c values from onset and zero resistivity, respectively. The solid triangles show the T_c values from the heat capacity. The solid and dashed lines are respectively the linear fit and the WHH fit to the data around the low-magnetic-field region of the diagram.

TABLE IV. Superconducting parameters of a single-crystalline sample of Ag_2Pd_3S.

T_c	2.25 K
γ	8.55 mJ/(mol K^2)
γ_n	7.02 mJ/(mol K^2)
γ_0	1.53 mJ/(mol K^2)
Θ_D	230 K
$\mu_0 H_{c2}(0)$	0.63 T
$\mu_0 H_c(0)$	0.018 T
κ_{GL}	25
$\xi(0)$	23 nm
$\lambda(0)$	568 nm
$\Delta C(T_c)/\gamma_n T_c$	1.50
$2\Delta/k_B T_c$	3.48
$\lambda_{\text{el-ph}}$	0.48

superconducting properties moderately, which superficially makes the system behave as a normal BCS superconductor like Li_2Pd_3B.

Contrarily, the observed H_{C2} vs T relationship (Fig. 6) does not seem to obey the BCS theory with simplified model assumptions. Although the theoretical calculation of the orbital limit of the critical field by Helfand and Werthamer [37] should give a convex curvature of T-dependent reduced critical field $h^*(T/T_C)$ around low temperatures ($T \ll T_C$), the actually observed T dependence rather looks like a T-linear behavior (heat-capacity data) or an upward tendency (resistivity onset-T_c data) even at 0.7 K($\sim$0.3 T_C). At a glance, it resembles the h^* curve for strongly coupled superconductors [39]; however, it is unlikely because the experimental results of specific heat jump at $T_C[\Delta C(T_C)/\gamma_n T_C \sim 1.50]$ and electron-phonon constant ($\lambda_{\text{el-ph}} \sim 0.48$) clearly suggests weak electron-phonon coupling in Ag_2Pd_3S. Werthamer Helfand, and Hohenberg expand their theory of h^* by taking a Pauli spin paramagnetic pair-breaking effect with a Maki parameter α and a spin-orbit scattering frequency λ_{SO} as perturbation into the orbital pair-breaking effect [38]. Their improved theory could successfully give more realistic H_{c2}-T curvature having a more plateaulike shape under high magnetic fields for some alloy superconductors; however, a curve thus obtained cannot reproduce such a straight data-set line observed in Ag_2Pd_3S even if α and λ_{SO} are adjusted to modest values. It can be expected that for Ag_2Pd_3S, orbital pair breaking essentially limits the actual H_{c2}, because the experimental $H_{c2}(0)$ value ($\sim$0.63 T) is much lower than the Pauli limit ($\mu_0 H_P(0) = 1.86 \times T_c \sim 4.2$ T), suggesting a small Maki parameter. The paramagnetic spin correction does not seem so much applicable to the case of Ag_2Pd_3S. A more realistic model in describing h^* may be required for understanding the T-linear behavior of $H_{c2}(T)$ in Ag_2Pd_3S. Presumably, additional factors unconsidered in the WHH theory, e.g., Fermi surface topology, gap anisotropy, and/or multigap structure, might be key factors to understand such a deviation of $H_{c2}(T)$ from the WHH theory. Kita and Arai have reported that h^* is enhanced significantly over the curve for the spherical Fermi surface (assumed in the WHH theory) with marked upward curvature [40,41]. This might be the most plausible case for Ag_2Pd_3S. At present, there is no definitive answer for the question of the unsat-

uration of H_{c2}. Further experimental and theoretical studies on Fermi surface shape and Maki parameters are expected to be helpful for deeper understanding of the critical field in Ag_2Pd_3S.

To clarify the detailed superconducting properties of Ag_2Pd_3S, microscopic experiments such as photoemission spectroscopy, NMR, or magnetic penetration depth measurements should be carried out. A variety of superconductors without inversion symmetry is desired in order to reveal the detailed physical properties of NCSCs. In particular, the fact that Ag_2Pt_3S, which is strongly related to the exotic superconductor Li_2Pt_3B, has a much larger ASOC than that of Ag_2Pd_3S must be a clue to help understand the unconventional properties of the NCSCs; actually, the preparation of the compound has been under way for some time. The theoretical and experimental studies on various NCSCs will reveal the novel and interesting physical properties of superconductors without inversion symmetry.

We successfully synthesized single crystals of the noncentrosymmetric superconductor Ag_2Pd_3S with a filled β-Mn structure and revealed the superconducting properties in terms of resistivity, magnetic susceptibility, heat capacity, and band calculations. Ag_2Pd_3S exhibits the superconducting transition at $T_c = 2.25$ K. The obtained superconducting parameters summarized in Table IV indicate that a type-II conventional weak-coupling BCS superconductivity with an isotropic gap is realized in Ag_2Pd_3S. On the other hand, temperature and field dependence of the T_c indicates that the superconductivity of Ag_2Pd_3S deviates from the normal BCS picture. Although an origin of the non-WHH shape in the H-T curve is still unclear, the understanding of superconducting properties of Ag_2Pd_3S plays an important role to study the weak ASOC effect on the compounds without inversion symmetry.

One of the authors (H.Y.) thanks Dr. K. Yamaura at the National Institute for Materials Science (NIMS) for fruitful discussions. H.Y. also thanks A. Sato at NIMS for his help with the single-crystal x-ray structural analysis. This work was supported by a Grant-in-Aid for Scientific Research from the Japan Society for the Promotion of Science (Grant No. 22-10454) and a Grant-in-Aid for Scientific Research (Grant No. 24740245) given by the MEXT, Japan.

[1] M. Smidman, M. B. Salamon, H. Q. Yuan, and D. F. Agterberg, Rep. Prog. Phys. **80**, 036501 (2017).
[2] V. M. Edel'stein, Zh. Eksp. Teor. Fiz. **95**, 2151 (1989) [Sov. Phys. JETP **68**, 1244 (1989)].
[3] L. P. Gor'kov and E. I. Rashba, Phys. Rev. Lett. **87**, 037004 (2001).
[4] E. Bauer, G. Hilscher, H. Michor, Ch. Paul, E. W. Scheidt, A. Gribanov, Yu. Seropegin, H. Noël, M. Sigrist, and P. Rogl, Phys. Rev. Lett. **92**, 027003 (2004).
[5] I. A. Sergienko and S. H. Curnoe, Phys. Rev. B **70**, 214510 (2004).
[6] P. A. Frigeri, D. F. Agterberg, and M. Sigrist, New J. Phys. **6**, 1 (2004).
[7] P. A. Frigeri, D. F. Agterberg, A. Koga, and M. Sigrist, Phys. Rev. Lett. **92**, 097001 (2004).
[8] V. P. Mineev, Phys. Rev. B **71**, 012509 (2005).
[9] V. M. Edelstein, Phys. Rev. Lett. **75**, 2004 (1995).
[10] S. Fujimoto, Phys. Rev. B **72**, 024515 (2005).
[11] N. Kimura, K. Ito, K. Saitoh, Y. Umeda, H. Aoki, and T. Terashima, Phys. Rev. Lett. **95**, 247004 (2005).
[12] T. Shibayama, M. Nohara, H. A. Katori, Y. Okamoto, Z. Hiroi, and H. Takagi, J. Phys. Soc. Jpn. **76**, 073708 (2007).
[13] K. Wakui, S. Akutagawa, N. Kase, K. Kawashima, T. Muranaka, Y. Iwahori, J. Abe, and J. Akimitsu, J. Phys. Soc. Jpn. **78**, 034710 (2009).
[14] H. Takeya, M. El Massalami, S. Kasahara, and K. Hirata, Phys. Rev. B **76**, 104506 (2007).
[15] T. Mochiku, H. Takeya, T. Wuernisha, K. Mori, T. Ishigaki, T. Kamiyama, H. Fujii, and K. Hirata, Physica C **445**, 57 (2006).
[16] R. Khasanov, I. L. Landau, C. Baines, F. La Mattina, A. Maisuradze, K. Togano, and H. Keller, Phys. Rev. B **73**, 214528 (2006).
[17] M. M. Doria, S. Salem-Sugui, Jr., P. Badica, and K. Togano, Phys. Rev. B **73**, 184524 (2006).
[18] H. Q. Yuan, D. Vandervelde, M. B. Salamon, P. Badica, and K. Togano, AIP Conf. Proc. **850**, 633 (2006).
[19] S. Tsuda, T. Yokoya, T. Kiss, T. Shimojima, K. Ishizaka, S. Shin, T. Togashi, S. Watanabe, C. Zhang, C. Chen, I. Hase, H. Takeya, K. Hirata, and K. Togano, J. Phys. Soc. Jpn. **78**, 034711 (2009).
[20] H. Q. Yuan, D. F. Agterberg, N. Hayashi, P. Badica, D. Vandervelde, K. Togano, M. Sigrist, and M. B. Salamon, Phys. Rev. Lett. **97**, 017006 (2006).
[21] M. Nishiyama, Y. Inada, and G.-Q. Zheng, Phys. Rev. Lett. **98**, 047002 (2007).
[22] A. Shimamura, Y. Furukawa, K. Kumagai, H. Takeya, and K. Hirata, Physica C **460**, 663 (2007).
[23] D. C. Peets, G. Eguchi, M. Kriener, S. Harada, Sk. Md. Shamsuzzamen, Y. Inada, G.-Q. Zheng, and Y. Maeno, Phys. Rev. B **84**, 054521 (2011).
[24] G. Eguchi, D. C. Peets, M. Kriener, S. Yonezawa, G. Bao, S. Harada, Y. Inada, G.-q. Zheng, and Y. Maeno, Phys. Rev. B **87**, 161203(R) (2013).
[25] H. R. Khan, H. Trunk, and Ch. J. Raub, J. Less Common Met. **30**, 167 (1973).
[26] R. E. Schaak, A. K. Sra, B. M. Leonard, R. E. Cable, J. C. Bauer, Y.-F. Han, J. Means, W. Teizer, Y. Vasquez, and E. S. Funck, J. Am. Chem. Soc. **127**, 3506 (2005).
[27] *SAINT and SADABS: Program for Data Collection and Absorption* (Bruker AXS Inc., Madison, Wisconsin, USA, 2007).
[28] G. M. Sheldrick, Acta Crystallogr. Sect. A Found. Crystallogr. **64**, 112 (2008).
[29] P. Blaha, K. Schwarz, G. K. H. Madsen, D. Kvasnicka, and J. Luitz, *WIEN2K, An Augmented Plane Wave + Local Orbitals Program for Calculating Crystal Properties* (Karlheinz Schwarz, Technische. Universitat, Wien, 2001).

[30] J. P. Perdew, K. Burke, and M. Ernzerhof, Phys. Rev. Lett. **77**, 3865 (1996).
[31] H. Kumagai and K. Inoue, Angew. Chem. Int. Ed. **38**, 1601 (1999).
[32] J. Kishine, K. Inoue, and Y. Yoshida, Prog. Theor. Phys. Suppl. **159**, 82 (2005).
[33] W. L. McMillan, Phys. Rev. **167**, 331 (1968).
[34] H. Takeya, K. Hirata, K. Yamaura, K. Togano, M. El Massalami, R. Rapp, F.A. Chaves, and B. Ouladdiaf, Phys. Rev. B **72**, 104506 (2005).
[35] K.-W. Lee and W. E. Pickett, Phys. Rev. B **72**, 174505 (2005).
[36] E. Helfand and N. R. Werthamer, Phys. Rev. **13**, 686 (1964).
[37] E. Helfand and N. R. Werthamer, Phys. Rev. **147**, 288 (1966).
[38] N. R. Werthamer, E. Helfand, and P. C. Hohenberg, Phys. Rev. **147**, 295 (1966).
[39] L. N. Bulaevskii, O. V. Dolgov, and M. O. Ptitsyn, Phys. Rev. B **38**, 11290 (1988).
[40] T. Kita and M. Arai, Phys. Rev. B **70**, 224522 (2004).
[41] M. Arai and T. Kita, J. Phys. Soc. Jpn. **73**, 2924 (2004).